INORGANIC CHEMISTRY FRONTIERS

RESEARCH ARTICLE

View Article Online
View Journal

Cite this: DOI: 10.1039/d6qi00542j

A rare-earth double perovskite ferroelastic for low-bias X-ray detection

Ze-Yu Jia,†[a,b] Zheng-Hui Hu,†[a,b] Hong-Fei Zhao,[a,c] Ting Hai,[a,b] Yi Wu,[a,b] Dong-Lan Zhang,*[c] Chang-Chun Fan,*[a,d] Yong Ai[e] and Chao Shi*[a,b]

Developing lead-free X-ray detection materials that combine high sensitivity, low operating voltage, and environmental friendliness poses a significant challenge in the field of radiation detection. In this study, we rationally designed and synthesized a three-dimensional rare-earth double perovskite, $(R\text{-3-FP})_2RbCe(NO_3)_6$ (**1**). **1** undergoes a first-order reversible ferroelastic phase transition around 400 K, primarily driven by the coordination distortion of Rb^+, the breaking of F–Rb bonds, and the cooperative disordering of guest ions, accompanied by dielectric responses and reversible domain structure evolution. Furthermore, **1** possesses a wide indirect bandgap of approximately 3.13 eV, which effectively suppresses dark current noise. First-principles calculations further reveal that the density of states distribution in the conduction and valence bands of its electronic structure facilitates carrier separation and transport, providing favorable conditions for X-ray photoelectric conversion. Building on this, we systematically evaluated the radiation detection performance of **1**. At a low bias voltage of 0.2 V, the device demonstrated a sensitivity of 184.5 μC Gy_{air}^{-1} cm^{-2} and a detection limit of 0.716 μGy_{air} s^{-1}, along with fast signal response and stability. This work not only reports on a distinct type of lead-free X-ray detection material based on ferroelastic phase transition behavior but also offers material design insights for developing low-power, high-stability X-ray detection devices.

Received 23rd March 2026,
Accepted 29th April 2026

DOI: 10.1039/d6qi00542j

rsc.li/frontiers-inorganic

1 Introduction

X-ray detection technology plays an indispensable role in key fields such as medical imaging, industrial non-destructive measurement, security inspection, and space radiation monitoring.[1,2] Among them, direct-type X-ray detection materials can directly convert high-energy photons into electrical signals, avoiding the information loss and noise amplification associated with the light conversion process in traditional indirect detection. Thus, they provide an ideal pathway for developing high-sensitivity, high-resolution, and low-power detection systems.[3–7] In recent years, organic–inorganic hybrid perovskite materials have made considerable progress in this field due to their strong X-ray attenuation capability, high carrier mobility–lifetime product, and excellent solution processability.[8–17] Lead-containing systems such as $MAPbI_3$ single crystals have demonstrated extremely high sensitivity (>10^6 μC Gy_{air}^{-1} cm^{-2}) and an ultralow detection limit.[18] However, the toxicity of lead and the environmental instability of halogen components limit their practical application and commercialization.[19–23] Consequently, lead-free double perovskites, such as $(NH_4)_3Bi_2I_9$, have been developed, achieving sensitivities on the order of 2.1×10^4 μC Gy_{air}^{-1} cm^{-2}.[24] Nevertheless, most existing high-performance detection devices rely on relatively high external bias voltages (typically >10 V) to achieve effective carrier separation and collection, which not only increases system energy consumption and thermal management burdens but also restricts their application prospects in portable, low-power devices.[25–27] Therefore, developing novel detection materials capable of operating at low bias voltages while combining high sensitivity, excellent stability, and environmental friendliness has become a critical and urgent challenge in this field.[28]

Among numerous emerging lead-free optoelectronic material systems, rare-earth double perovskites have garnered widespread interest in recent years due to their unique

[a]Jiangxi Province Key Laboratory of Functional Crystalline Materials Chemistry, Jiangxi University of Science and Technology, Ganzhou 341000, Jiangxi Province, P.R. China. E-mail: ccfanchem@jit.edu.cn, 13064147687@163.com
[b]Chaotic Matter Science Research Center, International Institute for Innovation, Jiangxi University of Science and Technology, Nanchang, Jiangxi Province, 330013, P.R. China
[c]School of Energy and Mechanical Engineering, Jiangxi University of Science and Technology, Nanchang, Jiangxi Province, 330013, P.R. China. E-mail: donglanzhangll@163.com
[d]School of Materials Engineering, Jinling Institute of Technology, Nanjing, Jiangsu Province, 211169, P.R. China
[e]Ordered Matter Science Research Center, Nanchang University, Nanchang, Jiangxi Province, 330013, P.R. China
†These authors contributed equally to this work.

structural tunability and excellent chemical stability, and the distinctive 4f electronic configuration and rich optoelectronic properties of rare-earth ions (*e.g.*, Ce^{3+} and Eu^{3+}).[29,30] In such materials, rare-earth ions and alkali metal ions (*e.g.*, Rb^{+} and Cs^{+}) jointly occupy the B-sites and can assemble various organic cations and anionic ligands (*e.g.*, NO_3^{-}) to construct diverse three-dimensional framework structures. Significantly, such crystalline frameworks may harbor structural phase transitions (*e.g.*, ferroelastic transitions) driven by coordination bond reorganization or ion ordering.[31,32] These phase transition processes are typically accompanied by significant changes in crystal symmetry, lattice stress, and dielectric properties, which may influence critical optoelectronic parameters such as carrier transport and noise background.[33,34] Although these materials have shown potential in fields like ferroelectrics and dielectrics, exploring their structural phase transition characteristics, investigating the intrinsic connection between such characteristics and X-ray detection performance, and subsequently developing novel detection materials remain research directions requiring in-depth exploration.[35–40]

Based on the above background, this study successfully designed and synthesized a novel three-dimensional rare-earth double perovskite, $(R\text{-3-FP})_2RbCe(NO_3)_6$ (**1**). This compound undergoes a first-order reversible ferroelastic phase transition around 400 K, accompanied by thermal hysteresis and reversible evolution of the domain structure. Through high- and low-temperature single-crystal X-ray diffraction analysis and local structural investigations, we revealed that its phase transition originates from multiple driving forces. Further investigations involving solid-state UV-Vis spectroscopy and density functional theory (DFT) calculations collectively confirmed that this compound possesses a wide indirect bandgap of approximately 3.13 eV. This feature is beneficial for suppressing thermally excited carriers, thereby reducing dark current noise. Building on this finding, we systematically evaluated its direct X-ray detection performance for the first time. The results demonstrate that devices fabricated from this material exhibit excellent comprehensive performance at extremely low bias voltages (0.2–5 V): at 0.2 V, the sensitivity reaches 184.5 μC Gy_{air}^{-1} cm^{-2}, the limit of detection is as low as 0.716 μGy_{air} s^{-1}, and the devices show good signal linearity, fast response characteristics, and cycling stability and fatigue resistance. Therefore, this study provides a paradigm for understanding and exploring the application potential of functional materials with structural phase transition characteristics in the field of radiation detection.

2 Experimental section

2.1 Synthesis

1 was synthesized *via* the slow evaporation method with a molar ratio of (R)-3-FP : $RbNO_3$: $Ce(NO_3)_3{\cdot}6H_2O$: HNO_3 = 2 : 1 : 1 : 6. The detailed procedure is as follows: First, (R)-3-fluoropyrrolidine (2 mmol, 0.178 g) was dissolved in 5 mL of deionized water. Then, under continuous stirring, HNO_3 (65 wt% aqueous solution, 6 mmol, 0.6 g) was added dropwise until complete dissolution was achieved. In a separate container, $RbNO_3$ (1 mmol, 0.147 g) and $Ce(NO_3)_3{\cdot}6H_2O$ (1 mmol, 0.434 g) were dissolved in another 5 mL portion of deionized water. The two solutions were subsequently combined and stirred continuously to yield a clear solution. After several days of slow evaporation at room temperature, colourless block-shaped single crystals of **1** were obtained. For **1**: calcd C 12.38%, H 2.08%, O 37.12%, N 14.44%; found C 12.34%, H 2.06%, O 37.13, N 12.92% (Table S8).

2.2 Characterization of physical properties

The structural and physical properties of **1** were characterized using multiple analytical methods in this study. The experimental techniques employed included variable-temperature powder X-ray diffraction (VT-PXRD), infrared spectroscopy (IR), thermogravimetric analysis (TGA), differential scanning calorimetry (DSC), single-crystal X-ray diffraction, variable-temperature dielectric measurements, polarized light microscopy (PLM) for ferroelastic domain observation, density functional theory (DFT) calculations, solid-state UV-Vis spectroscopy, and X-ray detection. Detailed descriptions of the experimental procedures and instrument parameters are provided in the SI.

3 Results and discussion

3.1 Phase transitions of 1

The IR spectrum of **1** displays characteristic features of its structure. Strong absorption bands at ~1600 cm^{-1} and ~1400 cm^{-1} are assigned to the asymmetric and symmetric stretching vibrations of the coordinated nitrate groups, respectively. The presence of a C–F stretching vibration at ~1080 cm^{-1} indicates the involvement of fluorine in coordination (Fig. S1). Additionally, absorptions in the low-frequency region (~500–400 cm^{-1}) confirm the formation of Ce–O and Rb–O bonds. The PXRD pattern shows complete agreement between the experimental profile and the simulated pattern based on the single-crystal structure, confirming the phase purity of the sample (Fig. S2). TGA indicates that **1** remains thermally stable up to approximately 503 K, thus ensuring that all subsequent physical property characterization studies are performed within a thermally stable regime (Fig. S3).

To systematically investigate the phase transition behavior of **1**, DSC was performed. Heating–cooling cycle measurements show a pair of reversible endothermic (heating) and exothermic (cooling) peaks near 400 K and 393 K, respectively (Fig. 1a), with a thermal hysteresis of about 7 K. Further verification by DSC at different scan rates reveals a good linear relationship between the hysteresis (ΔT) and the scan rate (Fig. 1b), a kinetic signature consistent with a first-order phase transition mechanism. To quantitatively characterize the thermodynamics of the phase transition, the enthalpy change (ΔH) and entropy change (ΔS) were calculated from the DSC data. The measured ΔH is approximately 4.80 kJ mol^{-1}, and the corresponding ΔS near 400 K is about 11.996 J mol^{-1} K^{-1}.

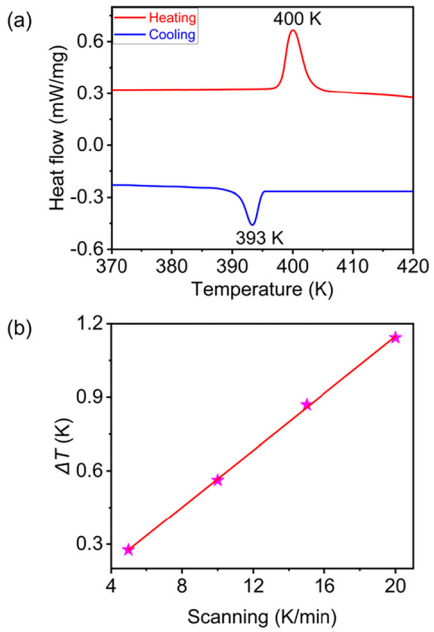

Fig. 1 (a) DSC curve of **1** measured at a heating/cooling rate of 10 K min^{-1} within the temperature range of 370–420 K. (b) ΔT variations at various scanning rates.

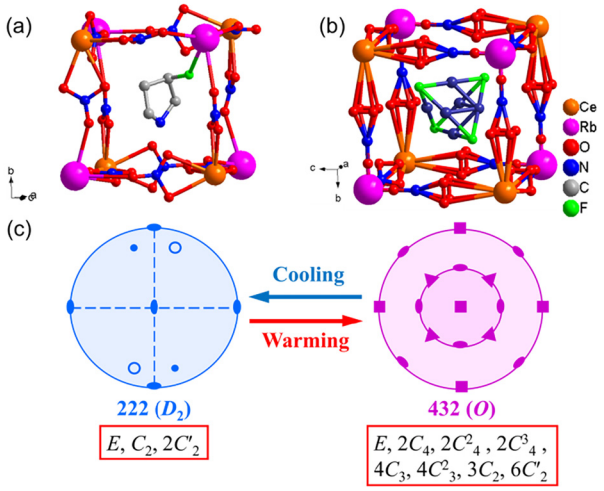

Fig. 2 (a) The three-dimensional framework structure of **1** in the LTP, where the circles highlight the coordination environment of Ce^{3+}/Rb^{+}. (b) The HTP structure of **1** exhibits a highly disordered and symmetric cubic framework. (c) The symmetry-breaking diagram of **1** at high and low temperatures is displayed.

Using the Boltzmann relation $\Delta S = R \ln N$, the estimated number of accessible configurations $N \approx 4.233$. This value represents the typical threshold for a conventional order–disorder phase transition, indicating an increase in configurational degrees of freedom during the transition, which corresponds to the order–disorder structural reorganization at the lattice or molecular level. Furthermore, repeated DSC cycling over five consecutive heating–cooling scans confirms the excellent reversibility and fatigue resistance of the phase transition (Fig. S4). To directly confirm the occurrence of the phase transition from a structural perspective, VT-PXRD measurements were conducted (Fig. S5). The results show clear changes in the positions and intensities of several diffraction peaks within the transition temperature range, including peak merging, splitting, or disappearance, indicating a change in crystal symmetry. This further confirms the existence of a structural phase transition from the viewpoint of long-range order. In summary, the combined physical characteristics of **1** near 400 K confirm that the process is a first-order solid–solid structural phase transition. These results provide a basis for understanding the underlying physical mechanism of the transition at the atomic scale.

3.2 Variable temperature structure of 1

To elucidate the reversible solid–solid phase transition mechanism of **1** at the atomic scale, the single-crystal structures of its low-temperature phase (LTP) and high-temperature phase (HTP) were systematically analyzed and compared.

In the LTP, **1** crystallizes in the orthorhombic space group $P2_12_12_1$ and exhibits a distorted three-dimensional framework structure (Fig. 2a). The Ce^{3+} centers adopt a typical hexacoordinate geometry, with all coordination sites occupied by oxygen atoms from six bidentate nitrate ligands, forming highly symmetric and rigid $[Ce(NO_3)_6]^{3-}$ coordination units. In contrast, the Rb^{+} cations display an unconventional coordination environment; they serve not only as nodes of the framework but also engage in Rb–F coordination interactions with terminal organic ligands. Specifically, six coordination sites of each Rb^{+} ion are occupied by oxygen atoms from bridging nitrate groups, which connect adjacent Ce^{3+} centers and extend the inorganic framework. The remaining two sites are coordinated by fluorine atoms from two (*R*)-3-fluoropyrrolidine ligands, forming relatively strong Rb–F bonds. Crucially, these fluorinated ligands act exclusively as terminal ligands and do not participate in framework extension. This combination of bridging nitrate oxygens and terminal F–Rb bonding imposes severe geometric constraints on the Rb^{+} coordination sphere, confining it to a distorted eight-coordinate configuration that stores considerable lattice strain.

The bond-length distortion index ΔD and bond angle variance σ^2 are quantitative measures of octahedral distortion. ΔD reflects the deviation of bond lengths from the average value, and σ^2 describes the spread of *cis* bond angles from 90°; larger values indicate greater distortion. Therefore, the degree of distortion in the coordination environment of Rb^{+} was quantified using concrete data.[41,42] The variance of the Rb–O bond lengths was determined to be 0.00481 $Å^2$, corresponding to a relative standard deviation of 2.39%. Significantly, the root-mean-square deviation of the O–Rb–O bond angles from the ideal octahedral values (90° and 180°) reaches 31.64°, indicating a severely distorted coordination polyhedron. This distorted, metastable configuration, rigidly confined by the framework, accumulates strain energy and thus provides an intrinsic driving force for the subsequent structural phase

transition. Furthermore, the two strong Rb–F coordination bonds act as additional anchoring points, further suppressing local structural flexibility. This feature may explain why **1** exhibits a relatively HTP temperature compared to many organic–inorganic hybrid materials dominated by hydrogen-bonding intermolecular interactions.

Upon heating HTP at 425 K, although the diffraction data quality is limited (R_1 = 0.265), a fundamental structural reorganization is still revealed (Fig. 2b). The space group transforms into cubic *F*432, indicating an increase in crystallographic symmetry. In this phase, the structural features are characterized by the cleavage of the F–Rb coordination bonds. The guest organic cations exhibit four-fold disorder, with their C and N atoms being coupled. Simultaneously, the nitrate ions display two-fold disorder. To further elucidate the nature of symmetrical evolution during the phase transition of **1**, we systematically analyzed its symmetry-breaking behavior (Fig. 2c). The heating process provides the necessary energy for structural reorganization, allowing the system to overcome the potential barrier for atomic rearrangement and thereby break the restricted symmetry of the LTP. During this process, symmetry operations that were "frozen" or suppressed in the original structure due to specific atomic positions and orientations—such as high-order rotation axes and mirror symmetries—are reactivated as thermal motion intensifies and coordination bonds rearrange. In the HTP, the structure reassembles based on dynamic disorder, resulting in a high-symmetry structure with a greater number of symmetry operations. This structural transformation is consistent with the characteristics of ferroelastic phase transitions among the 94 species.[43]

3.3 Thermodynamic behavior of 1

According to symmetry analysis, the phase transition of **1** satisfies the crystallographic requirements for a ferroelastic phase transition. Due to the poor quality of the high-temperature single-crystal diffraction data, polarized light microscopy was employed to experimentally verify the ferroelastic nature of the transition. At 303 K, the crystal exhibits birefringence under crossed polarizers, indicating the presence of ferroelastic domains in LTP (Fig. 3a). During heating, the ferroelastic domains persist in the LTP and remain visible until just before the phase transition. As the temperature approaches the transition point, the domain contrast gradually diminishes, and the ferroelastic domains completely disappear upon entering the HTP (Fig. 3b and c). In this paraelastic phase, the crystal becomes optically isotropic under crossed polarizers, a feature consistent with the restoration of higher crystallographic symmetry. Significantly, when the sample is subsequently cooled back to room temperature, the ferroelastic domains spontaneously reappear (Fig. 3d). The reversible emergence and disappearance of the domain patterns during the heating–cooling cycle provide direct evidence that domain formation is intrinsically associated with the structural phase transition. To further investigate whether the phase transition induces thermochromic behavior, the crystal color was observed under natural light during heating and cooling cycles across the transition temperature. No color change was observed (Fig. S6), confirming that **1** does not exhibit thermochromism, and the optical contrast changes in Fig. 3a–d are solely attributable to birefringence associated with ferroelastic domain evolution.

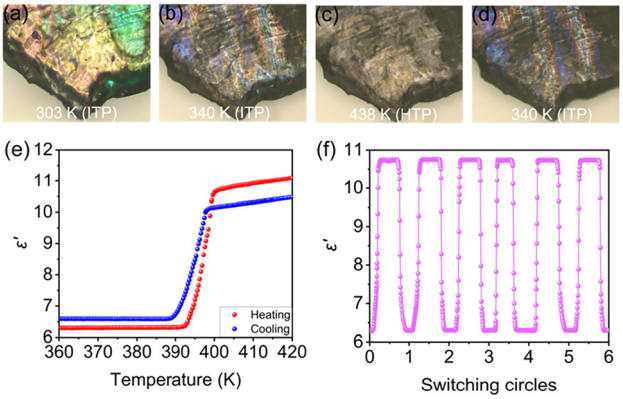

Fig. 3 (a–d) Evolution of the ferroelastic domain structures of **1** observed under a polarized light microscope at different temperatures. (e) Temperature dependence of the dielectric constant of **1** measured at a frequency of 1 MHz. (f) **1** exhibits switching response behavior in cyclic measurements, undergoing six consecutive switching cycles between high and low dielectric states.

Ferroelastic phase transitions are often accompanied by anomalous responses in dielectric properties due to the coupling between lattice distortion, symmetrical breaking, and polarization response. Therefore, we systematically investigated the dielectric response across the phase-transition temperature range. The temperature dependence of the real part of the dielectric constant (ε') for powdered **1** was measured at a frequency of 1 MHz (Fig. 3e). As the temperature increased and approached the phase-transition point, ε' exhibited an approximate twofold enhancement in dielectric response. This abrupt increase in dielectric response is consistent with the structural reorganization and symmetry change associated with the ferroelastic phase transition. To evaluate the reversibility and robustness of the dielectric response, repeated dielectric switching measures were performed. The dielectric anomaly near the phase-transition temperature was well preserved over six consecutive heating–cooling cycles, with no degradation in either the amplitude or position of the dielectric response (Fig. 3f). This result demonstrates the good fatigue resistance of **1**. In summary, these findings reveal a stable and reproducible dielectric response associated with the ferroelastic phase transition of **1**, highlighting the potential of such phase-transition materials for functional device applications.

3.4 X-ray response of 1

We first evaluated the fundamental optoelectronic properties of **1**, which form the basis of its X-ray detection capability. Solid-state ultraviolet-visible (UV-Vis) diffuse reflectance spectroscopy reveals an optical bandgap of approximately 3.31 eV (Fig. 4a), as determined by the Tauc plot for an indirect tran-

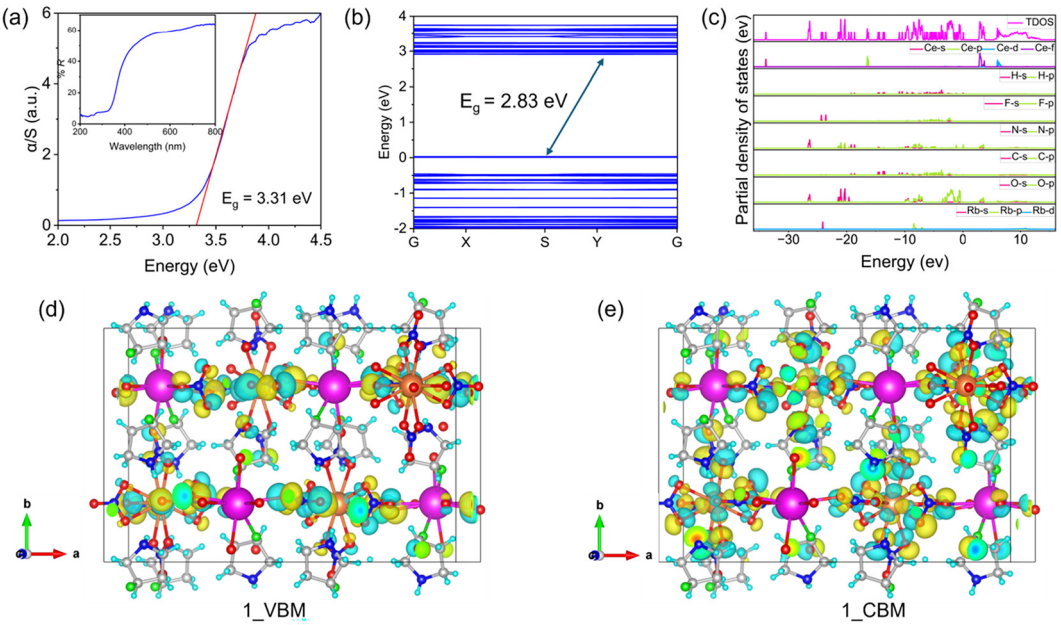

Fig. 4 (a) Solid UV-vis absorption spectra and bandgap diagram of **1**, (b) band structure of **1** calculated using density functional theory (DFT), (c) projected density of states (PDOS) diagram of **1**, (d and e) charge density distributions of the valence band maximum (VBM) and conduction band minimum (CBM) for **1**.

sition. To gain deeper insight into the electronic structure, density functional theory (DFT+U) calculations were performed without considering the magnetic ordering of Ce^{3+}. The computed bandgap is 2.83 eV (Fig. 4b), which is slightly lower than the experimental value—a well-known underestimation inherent to standard DFT functionals. Nevertheless, both experimental and theoretical results consistently confirm that **1** possesses a wide indirect bandgap, a critical feature for suppressing thermally generated dark current noise.

The partial density of states (PDOS) presented in Fig. 4c elucidates the orbital contributions near the Fermi level: the valence band maximum (VBM) is predominantly derived from the organic (*R*)-3-fluoropyrrolidine cations and the nitrate ligands, while the conduction band minimum (CBM) is dominated by the Ce 4f and 5d orbitals. To further visualize the nature of the photoexcitation process, we mapped the real-space charge density distributions of the VBM and CBM (Fig. 4d and e). The VBM charge density is highly localized on the nitrate ligands and organic cations, exhibiting characteristic ligand-centered behavior, whereas the CBM charge density is almost entirely concentrated on the Ce^{3+} center, demonstrating metal-centered characteristics. This pronounced spatial separation between electron and hole states directly confirms that the electronic excitation in **1** follows a ligand-to-metal charge transfer (LMCT) mechanism. Under X-ray irradiation, electrons are promoted from the nitrate/organic-dominated valence band to the Ce dominated conduction band, enabling efficient charge separation and effectively suppressing recombination. This charge-transfer characteristic, combined with its wide indirect bandgap, endows **1** with outstanding potential for low-noise, high-sensitivity X-ray detection.

Encouraged by the favorable optoelectronic properties of **1**, we proceeded to fabricate planar-type X-ray detectors based on **1** and conducted a systematic performance evaluation (inset of Fig. 5a). Based on the measured X-ray absorption coefficients (Fig. 5a), around an energy of 50 keV, the linear attenuation coefficient of **1** is comparable to that of silicon but lower than those of established compound semiconductor detector materials such as cadmium telluride (CdTe) and amorphous selenium (α-Se). This result indicates that although the X-ray absorption capability of **1** is not optimal, its absorption coefficient remains within the practical range for effective detection. More importantly, the subsequently demonstrated excellent charge carrier transport properties and extremely low noise background largely compensate for its relative deficiency in absorption, allowing the overall device to still exhibit outstanding detection potential. By measuring the transient photocurrent decay curves under X-ray excitation and fitting them based on the Hecht equation, the carrier mobility–lifetime product ($\mu\tau$) of compound **1** was determined to be approximately 3.6×10^{-4} cm^2 V^{-1} (Fig. 5b). This value surpasses those of most reported lead-free double perovskite systems, confirming the low defect density within the material and the long effective diffusion length and good electrode collection efficiency of photogenerated carriers, which form the key physical foundation for achieving charge extraction. Furthermore, current density–voltage (*J*–*V*) characteristic measurements under dark conditions (Fig. 5c) show that the current density of the device consistently remains on the order

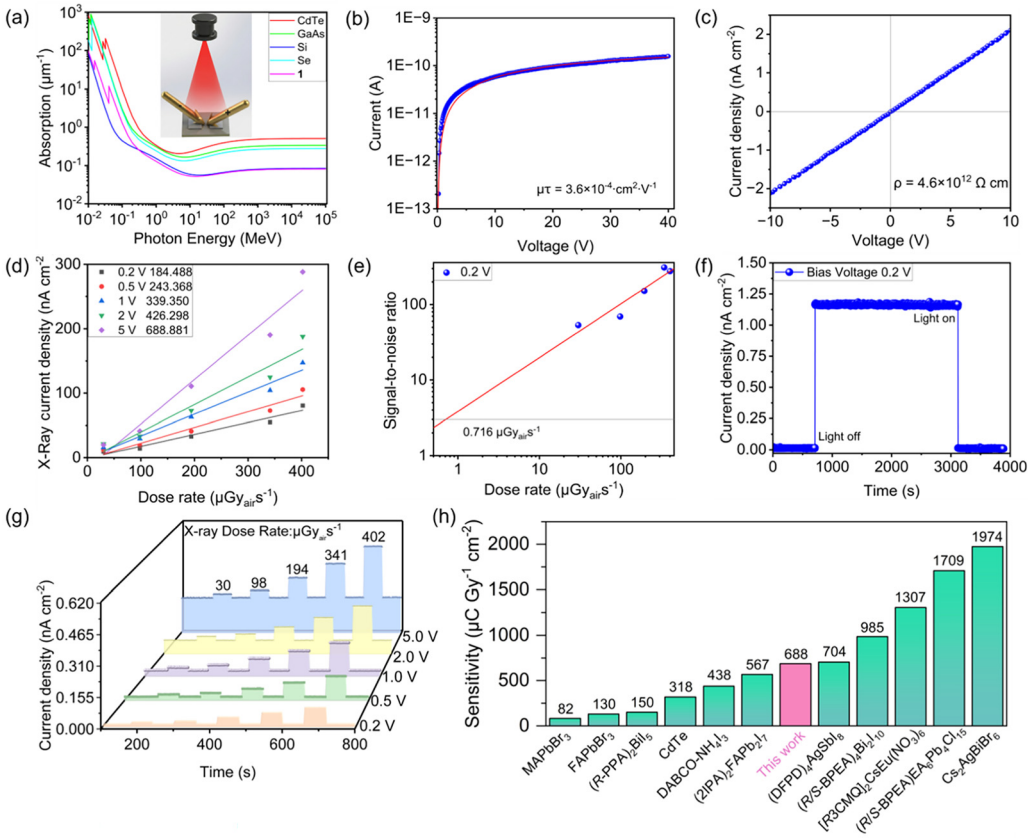

Fig. 5 X-ray detection performance of **1**. (a) Absorption coefficient of **1** compared to common semiconductor materials. The inset shows a schematic diagram of the simple electrode device structure. (b) Plot of $\mu\tau$ (carrier mobility–lifetime product) for **1** under X-ray excitation. (c) Resistivity curve of the **1** device under dark conditions. (d) Variation in device sensitivity at different bias voltages. (e) Signal-to-noise ratio (SNR) of the device as a function of X-ray dose rate under a 0.2 V bias voltage. The LOD determined by linear extrapolation (SNR = 3). (f) Long-term continuous operational stability measurement of the device under a 0.2 V bias voltage and a fixed dose rate. (g) Dynamic response curves of photocurrent density with increasing X-ray dose rate under different bias voltages. (h) Comparison of sensitivity between **1** and other reported X-ray detection materials at different operating bias voltages.

of nA cm^{-2}. Based on this, the resistivity of the material is calculated to be as high as ~4.6×10^{12} Ω cm. Such high resistivity directly reflects the extremely low free carrier concentration and excellent insulating properties of the material, which can effectively suppress dark current noise, establishing a crucial foundation for achieving high sensitivity and a low limit of detection in X-ray detection.[44–46]

Subsequently, we systematically measured the device's response performance to X-rays under different bias voltages (0.2 V, 0.5 V, 1 V, 2 V, 5 V). By varying the X-ray dose rate (from 5 to 400 $\mu Gy_{air}\ s^{-1}$), we recorded the corresponding changes in photocurrent density (Fig. 5g). At any fixed bias voltage, the photocurrent density shows a highly linear relationship with the incident X-ray dose rate, indicating excellent dose–response linearity and repeatability of the device. By linearly fitting the current density–dose rate curves, we calculated the device sensitivities at bias voltages of 0.2 V, 0.5 V, 1 V, 2 V, and 5 V to be 184.5, 243.4, 339.4, 426.3, and 688.9 μC $Gy_{air}^{-1}\ cm^{-2}$, respectively (Fig. 5d). This trend clearly demonstrates that as the applied electric field increases, the separation and collection efficiency of carriers improves, leading to a systematic enhancement in sensitivity. The limit of detection (LOD) is a key indicator for evaluating a detector's capability to detect weak signals. By analyzing the signal-to-noise ratio (SNR) corresponding to different X-ray dose rates at a 0.2 V bias, the LOD corresponding to SNR = 3 was determined to be 0.716 $\mu Gy_{air}\ s^{-1}$ (Fig. 5e). This low limit of detection indicates that even at an extremely low bias of 0.2 V, the device can reliably detect faint X-ray signals at the sub-microgray-per-second level, highlighting its application potential in low-dose imaging and radiation monitoring. The dynamic response characteristics and operational stability of the device are also crucial. In continuous cycling measurements exceeding 10^4 seconds, the device's photocurrent response remained stable with negligible signal attenuation or baseline drift (Fig. 5f). This result provides compelling evidence for the excellent fatigue resistance and environmental durability of both the material itself and the fabricated device.

Comparing the comprehensive performance of **1** within the context of current lead-free perovskites and broader X-ray

detection materials (Fig. 5h), its most prominent advantage lies in achieving excellent detection performance at extremely low operating voltages. Many reported high-performance detectors (such as some lead-based perovskites and traditional CdTe and α-Se detectors) typically require applied biases of 10 V or even hundreds of volts to achieve high sensitivity. In contrast, **1** can achieve comparable sensitivity (*e.g.*, 339.4 μC Gy_{air}^{-1} cm^{-2} at 1 V) under weak electric fields of ≤1 V. This characteristic endows it with irreplaceable application value in constructing next-generation radiation detection systems that are low-power, portable, and capable of long-term operation *via* miniature batteries, ultimately enabling efficient, stable, and reliable X-ray photoelectric conversion under nearly "power-free" weak electric fields.

4 Conclusions

This study successfully synthesized and systematically characterized a three-dimensional rare-earth double perovskite (R-3-FP)$_2$RbCe$(NO_3)_6$ (**1**). **1** exhibits a reversible ferroelastic phase transition. The material undergoes a first-order phase transition around 400 K, with its microscopic mechanism closely related to the coordination distortion of Rb^+ and the breaking of F–Rb bonds. Benefiting from its wide indirect bandgap, high carrier mobility–lifetime product, and high resistivity, **1** demonstrates excellent direct X-ray detection performance at extremely low operating voltages. At a bias voltage of only 0.2 V, the device achieves a sensitivity of 184.5 μC Gy_{air}^{-1} cm^{-2} and a detection limit of 0.716 μGy_{air} s^{-1}, while also exhibiting good stability over measurements exceeding 10^4 seconds. Compared to existing high-performance detectors that typically require higher operating voltages (>10 V), this material demonstrates comparable detection capabilities under weak electric fields of ≤1 V, highlighting its potential for applications in low-power, portable radiation detection devices. This work not only expands the material library of rare-earth double perovskites in the field of radiation detection but also provides an important example for exploring the relationship between structural phase transitions and optoelectronic functionality.

Author contributions

C. Shi: conceived the idea of the work; C.-C. Fan, Y. Ai and C. Shi: funding acquisition; Z.-Y. Jia and Z.-H. Hu: measurements, formal analysis, investigation, and writing – original draft; H.-F. Zhao: formal analysis and investigation; T. Hai and Y. Wu: data curation; D.-L. Zhang: DFT calculations; C.-C. Fan: measurement of X-ray response; Y. Ai: refinement of crystal structures; C. Shi: formal analysis, investigation, supervision, and writing – review & editing.

Conflicts of interest

The authors declare no conflict of interest.

Data availability

The data supporting this article have been included as part of the supplementary information (SI).

Supplementary information (SI) is available. See DOI: **https://doi.org/10.1039/d6qi00542j**.

CCDC 2526909 and 2526920 contain the supplementary crystallographic data for this paper.[47a,b]

Acknowledgements

This work was supported by the National Natural Science Foundation of China (No. 22175079), the Natural Science Foundation of Jiangxi Province (No. 20225BCJ23006, 20224ACB204002 and 20225BCJ23029), the Talent Introduction Project of Jinling Institute of Technology (JIT-B-202414) and the Open Project Program of Jiangxi Province Key Laboratory of Functional Crystalline Materials Chemistry, Jiangxi University of Science and Technology (2024SSY05161).

References

1 X.-L. Wu, A.-F. Li, M.-M. Yang, X. Hao, L.-L. Wu, R. Su and J.-Q. Zhang, Development of high-performance direct X-ray detector materials: from hybrid halide perovskites to all-inorganic lead-free perovskites, *J. Mater. Chem. C.*, 2024, **12**, 8647–8667.
2 M. Spahn, X-ray detectors in medical imaging, *Nucl. Inst. Methods Phys. Res. A.*, 2013, **731**, 57–63.
3 R. Chaudhari, C. R. Kant and A. Garg, Polymer-BiI_3 composites for high-performance, room-temperature, direct X-ray detectors, *MRS Commun.*, 2022, **12**, 358–364.
4 A. Datta, Z. Zhong and S. Motakef, A new generation of direct X-ray detectors for medical and synchrotron imaging applications, *Sci. Rep.*, 2020, **10**, 20097–20106.
5 Y. Cao, Y.-S. Ge, X. Sha, L.-Q. Meng, Y.-H. Gao, B. Li, X.-F. Yu and J. Li, Sensitive direct X-ray detectors based on the In–Ga–Zn–O/perovskite heterojunction phototransistor, *Flexible Printed Electron.*, 2022, **7**, 14013–14020.
6 B. Zhao, H.-W. Chen, Z.-Y. Zhu, X.-F. Yu, W.-X. Huang, S. Gao and Y.-L. Li, Polycrystalline lead-free perovskite direct X-ray detectors with high durability and low limit of detection via low-temperature coating, *ACS Appl. Mater. Interfaces*, 2024, **16**, 6113–6121.
7 X.-S. Geng, Y.-A. Chen, Y.-Y. Li, J. Ren, G.-H. Dun, K. Qin, Z. Lin, J.-L. Peng, H. Tian, Y. Yang, D. Xie and T.-L. Ren, Lead-free halide perovskites for direct X-ray detectors, *Adv. Sci.*, 2023, **10**, 2300256–2300281.
8 W. Qian, W.-T. Qiu, S.-S. Yu, D. Huang, R.-B. Lei, X.-Z. Huang, S. Xiao, X.-W. Wang and S.-H. Yang, Solvent engineering of $MAPbI_3$ perovskite thick film for a direct X-ray detector, *Nanoscale*, 2023, **15**, 6664–6672.

9 F.-G. Zhou, G.-Q. Peng, C. Shi, Z.-P. Ci, Z.-H. Li, Z.-W. Jin and Q. Wang, Polar isomer-driven cation-anion coupling enhances carrier dynamics and X-ray detectors sensitivity in 0D organic-inorganic hybrid Mn halides, *Adv. Funct. Mater.*, 2025, **36**, e13952–e13961.
10 Y. Hu, Y. Sha, L. Chen, Y.-F. Ma, Q. Huang, M. Zhang, P.-Y. Jia and Y.-H. Zhou, Bio-based adaptable dynamically cross-linked networks and their composites: multiple stimulus responses and potential electromagnetic shielding applications, *J. Mater. Chem. A.*, 2025, **13**, 4317–4328.
11 Y. Shen, C.-X. Ran, X. Dong, Z.-B. Wu and W. Huang, Dimensionality engineering of organic-inorganic halide perovskites for next-generation X-ray detector, *Small*, 2024, **20**, 2308242–2208265.
12 X.-L. Wu, A.-F. Li, M.-M. Yang, X. Hao, L.-L. Wu, R. Su and J.-Q. Zhang, Development of high-performance direct X-ray detector materials: from hybrid halide perovskites to all-inorganic lead-free perovskites, *J. Mater. Chem. C.*, 2024, **12**, 8647–8667.
13 H.-X. Cui, W.-J. Zhu, Y.-J. Deng, T.-X. Jiang, A.-X. Yu, H.-Y. Chen, S.-J. Liu and Q. Zhao, Lead-free organic-inorganic hybrid scintillators for X-ray detection, *Aggregate*, 2024, **5**, e454–e469.
14 M. P. A. Nanayakkara, M. G. Masteghin, L. Basiricò, I. Fratelli, A. Ciavatti, R. C. Kilbride, S. Jenatsch, T. Webb, F. Richheimer, S. Wood, F. A. Castro, A. J. Parnell, B. Fraboni, K. D. G. I. Jayawardena and S. R. P. Silva, Molecular weight tuning of organic semiconductors for curved organic-inorganic hybrid X-ray detectors, *Adv. Sci.*, 2022, **9**, 2101746–2101760.
15 X.-J. Zheng, W. Zhao, P. Wang, H.-R. Tan, M. I. Saidaminov, S.-J. Tie, L.-G. Chen, Y.-F. Peng, J.-D. Long and W.-H. Zhang, Ultrasensitive and stable X-ray detection using zero-dimensional lead-free perovskites, *J. Energy Chem.*, 2020, **49**, 299–306.
16 J.-W. Liu, Z.-K. Xu, T. Gan and Z.-X. Wang, Halogen Substitution Dual Regulation of Structure and Symmetry in an Edge-Shared ABX_3 Hybrid Ferroelectric, *Inorg. Chem.*, 2026, **65**, 6991–6998.
17 L.-P. Long, Z.-W. Huang, Z.-K. Xu, T. Gan, Y. Qin, Z.-W. Chen and Z.-X. Wang, H/F substitution activating tunable dimensions and dielectric-optical properties in organic lead-bromide hybrids, *Inorg. Chem. Front.*, 2024, **11**, 845–852.
18 Y.-L. Song, L.-Q. Li, M.-W. Hao, W.-H. Bi, A.-R. Wang, Y.-F. Kang, H.-M. Li, X.-H. Li, Y.-J. Fang, D.-R. Yang and Q.-F. Dong, Elimination of interfacial-electrochemical-reaction-induced polarization in perovskite single crystals for ultrasensitive and stable X-ray detector arrays, *Adv. Mater.*, 2021, **33**, 2103078–2103087.
19 Y. Zhou, J. Chen, O. M. Bakr and O. F. Mohammed, Metal halide perovskites for X-ray imaging scintillators and detectors, *ACS Energy Lett.*, 2021, **6**, 739–768.
20 W.-F. Fu, A. G. Ricciardulli, Q. A. Akkerman, R. A. John, M. M. Tavakoli, S. Essig, M. V. Kovalenko and M. Saliba, Stability of perovskite materials and devices, *Mater. Today*, 2022, **58**, 275–296.
21 N. Moody, S. Sesena, D. W. Dequilettes, B. D. Dou, R. Swartwout, J. T. Buchman, A. Johnson, U. Eze, R. Brenes, M. Johnston, C. L. Haynes, V. Bulovi and M. G. Bawendi, Assessing the regulatory requirements of lead-based perovskite photovoltaics, *Joule*, 2020, **4**, 970–974.
22 L.-Q. Mei, R.-X. Xie, S. Zhu, S.-L. Deng, H.-W. Xu, X.-T. Fan, W.-Y. Yin and Z.-J. Gu, Neurotoxicity study of lead-based perovskite nanoparticles, *Nano Today*, 2023, **50**, 101830–101844.
23 Q. Wali, F. J. Iftikhar, M. E. Khan, A. Ullah, Y. Iqbal and R. Jose, Advances in stability of perovskite solar cells, *Org. Electron.*, 2020, **78**, 105590–105606.
24 W. Wei, Y. Zhang, Q. Xu, H.-T. Wei, Y.-J. Fang, Q. Wang, Y.-H. Deng, T. Li, A. Gruverman, L. Cao and J.-S. Huang, Monolithic integration of hybrid perovskite single crystals with heterogenous substrate for highly sensitive X-ray imaging, *Nat. Photonics*, 2017, **11**, 315–321.
25 Z.-Z. Li, F.-G. Zhou, H.-H. Yao, Z.-P. Ci, Z. Yang and Z.-W. Jin, Halide perovskites for high-performance X-ray detector, *Mater. Today*, 2021, **48**, 155–175.
26 M. H. Miah, M. U. Khandaker, M. A. Islam, M. Nur-E-Alam, H. Osman and M. H. Ullah, Perovskite materials in X-ray detection and imaging: recent progress, challenges, and future prospects, *RSC Adv.*, 2024, **14**, 6656–6698.
27 Z.-Y. Zhu, H.-W. Chen, W.-X. Huang, B. Zhao, S. Gao, Y. He, G.-K. Zhong, X.-Q. Yang, X.-Z. Wang and Y.-L. Li, Ion leakage current control for polycrystalline metal halide perovskite direct X-ray detectors, *ACS Appl. Mater. Interfaces*, 2024, **16**, 53177–53185.
28 H. Li, Y. Wu, Q.-W. Guan, C.-M. Ji, H. Ye, Z.-Y. Wu, S. Chen, C.-S. Zhang, Y. Li, H. Liu and J.-H. Luo, Bimetallic Co-occupation and multiple interlayer interactions in aromatic double perovskite for highly sensitive and stable self-driven X-ray detection, *Adv. Mater.*, 2025, **38**, e11539–e11546.
29 C. Shi, L. Ye, Z.-X. Gong, J.-J. Ma, Q.-W. Wang, J.-Y. Jiang, M.-M. Hua, C.-F. Wang, H. Yu, Y. Zhang and H.-Y. Ye, Two-dimensional organic-inorganic hybrid rare-earth double perovskite ferroelectrics, *J. Am. Chem. Soc.*, 2020, **142**, 545–551.
30 C. Shi, J.-J. Ma, J.-Y. Jiang, M.-M. Hua, Q. Xu, H. Yu, Y. Zhang and H.-Y. Ye, Large piezoelectric response in hybrid rare-earth double perovskite relaxor ferroelectrics, *J. Am. Chem. Soc.*, 2020, **142**, 9634–9641.
31 H.-F. Zhao, Z.-H. Hu and H. Liang, A Tb^{3+} -based hybrid rare-earth double perovskite with ferroelastic switching and long photoluminescence lifetime, *Inorg. Chem.*, 2025, **64**, 25305–25310.
32 H.-K. Li, L.-P. Wang, Z.-Z. Cui, Q. Xu, L.-L. Zou, N. Wang, L.-P. Miao, H.-Y. Ye and C. Shi, A series of bimetallic ammonium RbEu nitrates exhibiting switchable dielectric constant and photoluminescence properties, *J. Mater. Chem. C.*, 2024, **12**, 14122–14128.
33 J.-C. Qi, Y. Qin, H. Peng, H.-P. Lv, Y.-J. Bai, X. Shen, Z.-T. Xia and W.-Q. Liao, A Z/E isomeric cation designed organic-inorganic cadmium chloride ferroelectric with broadband white-light emission, *Sci. China:Chem.*, 2024, **67**, 4167–4174.

34 Z.-H. Hu, H.-F. Zhao and H. Liang, Hybrid rare-earth double perovskite based on K(I)/Pr(III) exhibiting two isostructural phase transitions, switchable dielectric properties, and long fluorescence lifetime, *Inorg. Chem. Commun.*, 2026, **184**, 115903–115908.
35 H.-Y. Zhang, Y.-Y. Tang, Z.-X. Gu, P. Wang, X.-G. Chen, H.-P. Lv, P.-F. Li, Q. Jiang, N. Gu, S.-Q. Ren and R.-G. Xiong, Biodegradable ferroelectric molecular crystal with large piezoelectric response, *Science*, 2024, **383**, 1492–1498.
36 D.-X. Feng, Y. Mu, J. Li, S.-D. Han, J.-H. Li, H.-L. Sun, M. Pan, J.-X. Hu and G.-M. Wang, Light-induced electron transfer toward on/off room temperature phosphorescence in two photochromic coordination polymers, *Adv. Funct. Mater.*, 2023, **33**, 2305796–2305803.
37 Z.-T. Xia, H.-P. Chen, J.-C. Qi, H. Peng, X. Shen, Y.-J. Bai, Z.-Y. Wang, T.-E. Yang and W.-Q. Liao, A high phase transition temperature organic-inorganic Sn(IV)-based metal halide designed by applying amino positional isomerism to the cation, *Inorg. Chem. Front.*, 2025, **12**, 2825–2832.
38 H.-Y. Zhang and R.-G. Xiong, Ferroelectric polymers take a step toward bioelectronics, *Science*, 2023, **381**, 484–485.
39 Z.-K. Xu and Z.-X. Wang, A low-dimensional ferrocenium lead-iodide perovskite ferroelastic with a narrow band gap, *Chem. Commun.*, 2025, **61**, 15810–15813.
40 Z.-Y. Yu, G.-F. Li, Z.-K. Xu, L. Long, Y. Qin, Z.-Y. Du and Z.-X. Wang, Enantiomeric organic amine-borane adduct crystals with room-temperature multi-channel switches, *Chin. J. Struct. Chem.*, 2025, **44**, 100715–100721.
41 Y.-M. Song, Y.-F. Zhou, C.-C. Chen, K.-Z. Fan, Z. Wang, Y. Guo, Z.-M. Chen, L.-L. Mao, J. Yin and P. C. Y. Chow, Structure–emission property relationship of bilayer 2D hybrid perovskites, *J. Am. Chem. Soc.*, 2025, **147**, 19902–19910.
42 Y.-H. Mao, S.-H. Guo, X. Huang, K.-J. Bu, Z.-Y. Li, P. Q. H. Nguyen, G. Liu, Q.-Y. Hu, D.-Z. Zhang, Y.-P. Fu, W.-G. Yang and X.-J. Lü, Pressure-modulated anomalous organic–inorganic interactions enhance structural distortion and second-harmonic generation in $MHyPbBr_3$ perovskite, *J. Am. Chem. Soc.*, 2023, **145**, 23842–23848.
43 K. Aizu, Possible species of "ferroelastic" crystals and of simultaneously ferroelectric and ferroelastic crystals, *J. Phys. Soc. Jpn.*, 1969, **27**, 387–396.
44 H.-T. Wei, Y.-J. Fang, P. Mulligan, W. Chuirazzi, H.-H. Fang, C.-C. Wang, B. R. Ecker, Y.-L. Gao, M. A. Loi, L. Cao and J.-S. Huang, Sensitive X-ray detectors made of methylammonium lead tribromide perovskite single crystals, *Nat. Photonics*, 2016, **10**, 333–339.
45 L.-S. Liu, M.-X. Xu, X.-G. Xu, X.-T. Tao and Z.-L. Gao, High sensitivity X-ray detectors with low degradation based on deuterated halide perovskite single crystals, *Adv. Mater.*, 2024, **36**, 2406443–2406454.
46 C.-F. Wang, H.-J. Li, C. Ning, L. Wang, Q.-F. Luo, T.-L. Li, H.-F. Ni, Z.-F. An, Z.-X. Zhang, J.-L. Wang, D.-W. Fu, M.-G. Ju, K. Zhao and Y. Zhang, Eco-friendly preparation of high-quality lead-free halide ferroelectric solid-solution toward high-performance X-ray detection, *Angew. Chem., Int. Ed.*, 2026, **65**, e25694–e25706.
47 (*a*) CCDC 2526909: Experimental Crystal Structure Determination, 2026, DOI: **10.5517/ccdc.csd.cc2qtg67**; (*b*) CCDC 2526920: Experimental Crystal Structure Determination, 2026, DOI: **10.5517/ccdc.csd.cc2qtgkl**.